JMEPEG (2023) 32:9263–9278
https://doi.org/10.1007/s11665-022-07780-7

1059-9495/$19.00

TECHNICAL ARTICLE

Investigation of Microstructure and Several Quality Characteristics of AA7075/Al_2O_3/Coconut Shell Ash Hybrid Nano Composite Prepared through Ultrasonic Assisted Stir-Casting

Ashish Kumar, R.C. Singh, and Rajiv Chaudhary

Submitted: 17 June 2022 / Revised: 29 November 2022 / Accepted: 4 December 2022 / Published online: 27 December 2022

The present study focuses on the investigation of mechanical, thermal, and corrosion behaviors of cast hybrid nano-metal matrix composites of AA7075 with Al_2O_3 and coconut shell ash (CSA) nano- and micro-sized particulates, respectively, as reinforcements. Using an ultrasonic assisted stir-casting technique, the hybrid composites were fabricated using 2, 4, and 6% by weight of CSA and 0.5% by weight of Al_2O_3 in equal proportions. SEM, EDS, XRD, porosity, tensile, damping, dislocation density, coefficient of thermal expansion, and polarization tests were used to characterize four different combinations. The findings indicated that the nano- and micro-sized particulates were spread evenly in the matrix. The dislocation density, which is caused by a thermal mismatch between the matrix and the reinforced particles, as well as composite porosity, have been found to have a significant impact on the damping behaviors of hybrid composites. Also, the thermal expansion coefficient of HMMCs decreased with the addition of Al_2O_3 and CSA. The corrosion resistance was gradually increased by increasing the weight percentage of reinforcement in the AA7075 matrix.

Keywords corrosion, damping characteristics, dislocation density, hybrid composite, nano-reinforcement, thermal property

1. Introduction

Hybrid metal matrix composites (HMMCs) were developed to improve the performance of composites that were previously restricted to single reinforcement. In a hybrid metal matrix, two or more synthetic ceramics are added to a metal matrix. Carbides, oxides, and borides could be used as ceramic particles to reinforce the aluminum matrix (Ref 1-3). The most widely employed reinforcing materials are alumina (Ref 4), silicon carbide (Ref 5), boron carbide (Ref 6), and graphite (Ref 7), among others. Moreover, aluminum oxide and graphite particles made from these are more affordable. The desirable properties, like the flexible coefficient of thermal expansion and the solid lubricating characteristic, render these reinforcement particle forms suitable for producing components such as engine bearings, cylinder liners, pistons, and piston rings (Ref 8-12). The present scenario in the fabrication of hybrid composite is reinforcing agriculture waste (secondary reinforcement) with synthetic ceramic (primary reinforcement) (Ref 9). The broad applicability of such hybrid composites has attracted the attention of researchers who have designed and conducted experiments to develop superior and cost-efficient MMCs. Several good attempts have been made at producing MMCs from industrial wastes like graphite (Ref 7), fly ash (Ref 6), red mud (Ref 13), and the ashes of agricultural wastes like bagasse ash (Ref 14), coconut shell ash (Ref 15), corn cob (Ref 16), basalt fibers (Ref 17), coconut shell char (Ref 18), maize stalk (Ref 19), and rice husk ash (Ref 20). The advantages of including CSA are ease of access, low cost, low density, and lower pollution (Ref 21). According to the literature review, AMCs with CSA play a significant role in the progress of HMMCs due to their improved mechanical behaviors and widespread applications in a variety of fields. However, reinforcing natural ceramic is insufficient to improve the composite's quality characteristics. As a result, it's been combined with synthetic ceramic to increase mechanical, corrosion, and tribological properties.

In current scenario, nano-sized reinforcing particulates are being utilized in the metal matrix nanocomposite (MMnC). The use of nanoscale reinforced particulates at matrix interfaces provides a larger surface area, which results in improved composite properties like fatigue life, mechanical strength, and creep resistance at high temperatures without any loss of ductility (Ref 15, 22-25). The sizes, shapes, distribution of particulates, thermal stability, and hardening mechanism of nano-reinforcement materials have a significant impact on the final characteristics of MMnCs (Ref 23). The most difficult issue in the stir-casting method for processing MMnCs is achieving uniform reinforcement dispersion. The significant variability in densities between nanoparticles and molten

Ashish Kumar, Department of Mechanical Engineering, Delhi Technological University, New Delhi, Delhi 110042, India; and Galgotias College of Engineering and Technology, Greater Noida 201306, India; and **R.C. Singh** and **Rajiv Chaudhary**, Department of Mechanical Engineering, Delhi Technological University, New Delhi, Delhi 110042, India. Contact e-mail: ashuatcoer@gmail.com.

matrix, as well as the significantly higher specific surface area, results in lower wet-ability. Some authors improve the wetting properties of nano-reinforcements by combining stir casting and an ultrasonic effect during casting, which results in reinforcement agglomeration breaking (Ref 26). In MMnCs, micro-size ceramic particles are combined with nano-size reinforcements, and improved results in terms of quality attributes have been documented as compared to micro-size particles-reinforced MMCs (Ref 15, 27). Because of their superior characteristics over single-reinforced composites, hybrid nano-metal matrix composites (HnMMC) are being studied by researchers all over the world. To ensure the precise behavior of such materials, the damping capacity (Ref 28-30), thermal expansion (Ref 31), and corrosion resistance (Ref 32-34) must be monitored.

Numerous crucial alloys and metals have limited damping capacities, making them unsuitable for use in dynamic structures. Though, by adding reinforced particulates with better damping capacities to form MMCs, it is promising to get better damping capability from such materials (Ref 30). Although the aluminum alloys show low damping behavior, they are nevertheless used because of their higher strength-to-density ratio. By adding SiC to AlSi, Madeira et al. (Ref 29) increased its damping capacity. The reduction in thermal expansion coefficient indicates superior dimensional stability, which can be achieved by incorporating reinforced particulates into AMCs. Several efforts have been made to investigate the microstructure, mechanical, and wear behavior of various reinforced particulates included with AA7075 (Ref 6, 7, 9, 11, 15, 26). The coefficient of thermal expansion Al-Mg-AA535 composites reinforced with fly ash was found to reduce with an enhancement in the content of fly ash. Corrosion of materials is a serious issue in the aircraft and shipping industries, as it can occur in a variety of locations throughout the structure. Localized corrosions such as crevice, pitting, intergranular, and exfoliation can occur in various parts of AA7xxx series aircraft. Corrosion is a severe issue in older airplanes; intergranular (IGC), pitting, exfoliation, and crevice corrosion are examples of confined corrosion. They arise at various points in wing structures through AA7xxx (Ref 33).

The novelty of this study is that it looks at the mechanical, damping, dislocation density, coefficient of thermal expansion, and corrosion behaviors in depth; these qualities are critical for materials used in airplanes, automobiles, and ships. This type of investigation would be extremely beneficial in assisting in the efficient design of Al7075/Al_2O_3/CSA hybrid composites as well as the precise prediction of their mechanical and corrosion characteristics.

2. Materials and Methods

AA7075 is an imperative material for industrial purposes, hence its selection as the matrix material. Micro-sized (40-60 μm) CSA and nano-sized (40-90 nm) alumina particles were selected for the reinforcement. The chemical analysis of AA7075 reveals the weight percentage of major elements such as Zn (5.31), Cu (1.13), Mg (2.12), Si (0.41), Fe (0.52), Mn (0.29), Ti (0.22), Cr (0.18), and balance Al. The XRF oxide analysis of CSA particles reveal the weight percentages of main oxides such as SiO_2 (46.35), Fe_2O_3 (18.80), Al_2O_3 (20.85), MgO (13.15), Na_2O (0.85), CaO (0.62), ZnO (0.31), and others. The morphology and particle size of nanoscale Al_2O_3 powder were determined using a transmission electron microscope (TEM). Approximately 10 mg/L of alumina nanoparticles were immersed in an acetone solution, followed by 4-5 min of ultrasonic treatment. Figure 1(a), (b), (c), and (d) shows the TEM analysis of alumina particles and the SEM analysis of CSA particulates, respectively. Based upon previous research work, the range of reinforcement (alumina and CSA) was finalized. The preheated (up to 250 °C) CSA was ultrasonically assisted stir-cast into the base aluminum alloy 7075 matrix to achieve uniform wettability and homogeneous mixing, resulting in better bonding among the AA7075 matrix.

Figure 2 shows the experimental setup of the ultrasonic assisted stir-casting process. As per previous literature (Ref 26), a preheated mechanical stirrer having a graphite impeller was used to generate vortex motion in a molten melt to ensure uniform mixing. At the same time, the preheated (200 °C) nano-alumina particles were mixed well with pure aluminum powder and added at a constant feed rate. During the process of melting, about 10 g of Na_3AlF_6 was mixed into the molten melt to avoid slag formation and to enhance the casting efficiency. A synchronized motor was used to rotate the mechanical impeller between 500 and 700 rpm during the process of addition. It is evidence of the homogeneous dispersion of the reinforcement during the molten melt.

The melt temperature was kept at 800 °C for another 6 min after adequate stirring of the molten slurry. After dipping a titanium waveguide into the molten metal and ultrasonically treating it for 6 min to break up the bigger clusters, the sonication process was prolonged for another 6 min to remove any remaining agglomerations, degas, and improve the matrix grain size. Instantly after the achievement of the addition of the reinforced particles into the molten melt slurry, it was cast into the preheated (500 °C) mold of gray cast iron. Three dissimilar combinations of hybrid composites and AA7075 alloy without reinforcement were fabricated. Each combination of hybrid composite contains 0.5% Al_2O_3 by weight in an equal proportion. CSA0, CSA2, CSA4, and CSA6 are the codes for samples with 0, 2, 4, and 6 weight percentages of CSA, respectively. A wire electro-discharge machine (WEDM) was used for the fabrication of the test specimen.

2.1 Metallographic Studies

OM and SEM were used to examine the microstructure of the produced samples at the micron level. Polishing is performed on the prepared samples by global metallurgical processes. The next step is an etching, which is done with Keller's reagent on all of the samples. Optical metallographic and SEM images were analyzed to examine the finished surfaces. EDS and XRD analyses have been done for confirmation of the existence of constituent phases and elements in the developed composite.

2.2 Mechanical, Damping, Thermal and Corrosion Tests

Experimental density was determined by the Archimedes' principle. In this method of density measurement, the specimen is weighed in air and another fluid of known density. The rule of mixture (ROM) method was used to find the experimental and theoretical densities. The variation of theoretical density and experimental density gives the porosity in the fabricated composites. A universal testing machine (UTM) was employed to examine the tensile behaviors of the developed hybrid

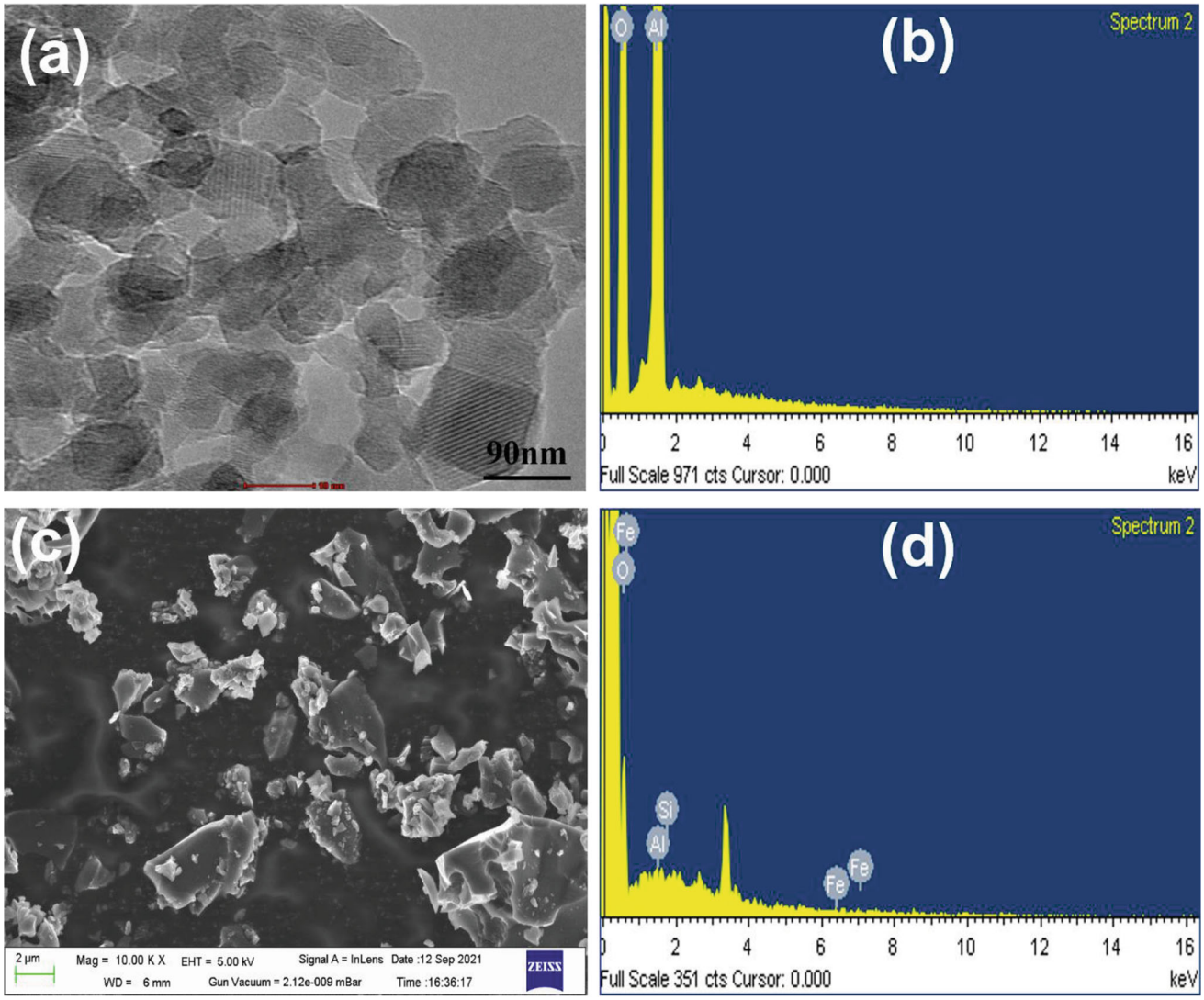

Fig. 1 (a), (b) TEM analysis of nano-alumina powder and (c), (d) SEM morphology of CSA particulates

composite for tensile response. The samples were prepared as per the ASTM-E8 standard, and the tensile test was done under room temperature at 100 kN. The elongation of specimens was tested in an additional test at a uniform strain rate of 0.25 mm/s. On each combination, four tests were done, and the average value of the ultimate tensile strength (UTS), elastic modulus (E), and ductility test findings was used in the computation. Using a 3-point bending machine, the damping behavior of as-cast composites was investigated (i) with varying loading frequencies (5-20 Hz) at constant strain (2.5-6 m) and (ii) with varying temperature in the range of 20 to 200 °C by using a constant heating rate and cooling rate of 5 and 8 °C/min, respectively. The damping behaviors were measured using a specimen with dimensions (60 mm × 10 mm × 2.5 mm). Each sample's damping capacity was calculated in terms of tan δ (Ref 30). The coefficient of thermal expansion (CTE) computed by the thermal–mechanical analyzer (TMA) of the fabricated hybrid composite specimens. A load of 0.05 N was applied to perform thermal expansion measurements in the temperature range of 25-275 °C under a nitrogen gas atmosphere. Corrosive solutions were made with 35 g of sodium chloride solution in 1 L of distilled water. The dimension of corrosion sample is (9 × 9 × 9) mm^3 in size, and it is metallographically polished to produce an electrode. In a 3.5% sodium chloride solution, the samples were evaluated for 5 h and 7 days. To find out the corrosion nature of the specimens, the linear potentiodynamic polarization (LPP) method was used (Ref 33). In the presence and absence of inhibitors, AA7075 and hybrid composite specimens were tested using anode and cathode polarization in sodium chloride solution. The corrosion potential, linear polarization resistance, and corrosion current were calculated.

3. Results and Discussion

3.1 Microstructural Study

Figure 3(a), (b), (c), and (d) depicts the microstructure of monolithic alloy AA7075 and Al_2O_3/CSA-based hybrid composite specimens. The homogeneous dispersion of reinforced particles in the matrix is depicted in Fig. 3(b), (c), and (d). The intermetallic phases like $MgZn_2$, Mg_2Si, $Al_{13}Fe_4$, and Al_2CuMg may be formed during the solidification of AA7075 (Ref

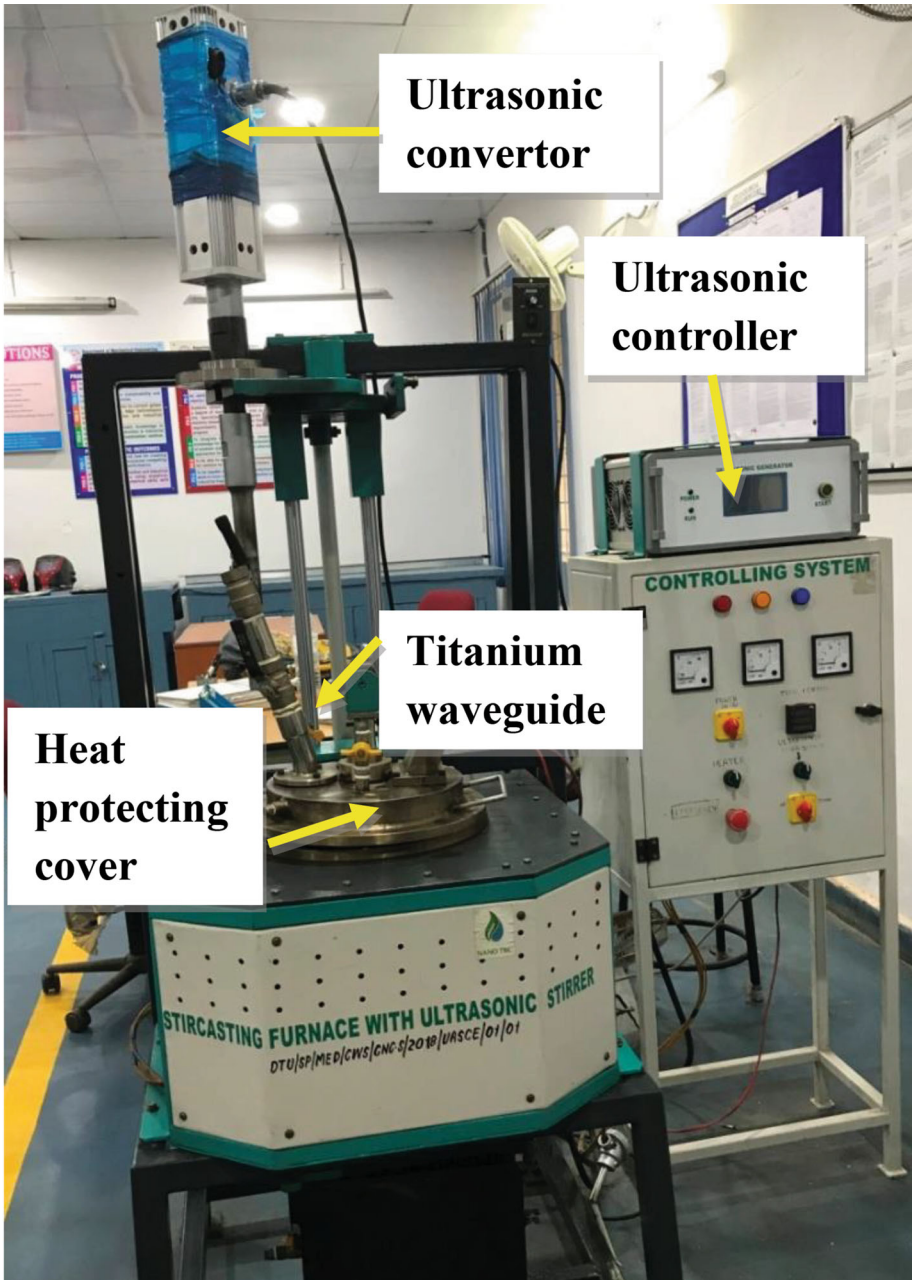

Fig. 2 Experimental setup of ultrasonic assisted stir-casting

9). Figure 3(a) depicts the homogeneous distributions of $MgZn_2$ phase with fine grain. The maximum level of porosity is clearly shown in Fig. 3(d). Grain refinements occur as the percentage of reinforcement increases, as shown in Fig. 3(c) and (d).

SEM imaging of AA7075 and developed composite specimens is shown in Fig. 4(a), (b), (c), and (d). The existence of nearly continuous intermetallic phases in the inter-dendritic zones is revealed by a SEM micrograph of the monolithic alloy (Fig. 4a). The critical analysis of the inter-dendritic region reveals the creation of at least two distinct types of intermetallic phases, one with bright contrast and high Zn content, and a different with shaded contrast and low Zn content but high Cu content. In the base alloy 7075, the formation of β-phase or secondary phase was discovered. However, this period was limited (Ref 35). As shown in Fig. 4(b), the AA7075 matrix had a homogeneous distribution of nano-sized Al_2O_3 and micro-sized CSA particles. Moreover, the fabricated composite has very few defects that recognize the interface of reinforced particulate and matrix. Furthermore, the SEM spectra in Fig. 4(c) and (d) confirmed that there is a slight indication of accumulation or clustering of Al_2O_3 and CSA particulates in the developed composite, which proved a sound casting process.

Figure 5(a), (b), (c), and (d) shows the EDS analysis of composites CSA2, CSA4, and CSA6, which confirm the presence of alloying elements and reinforcement (Al_2O_3 and CSA). The peaks of Al, Zn, Si, O_2, and Fe, etc., are detected in energy dispersive spectra, which are evidence of the presence

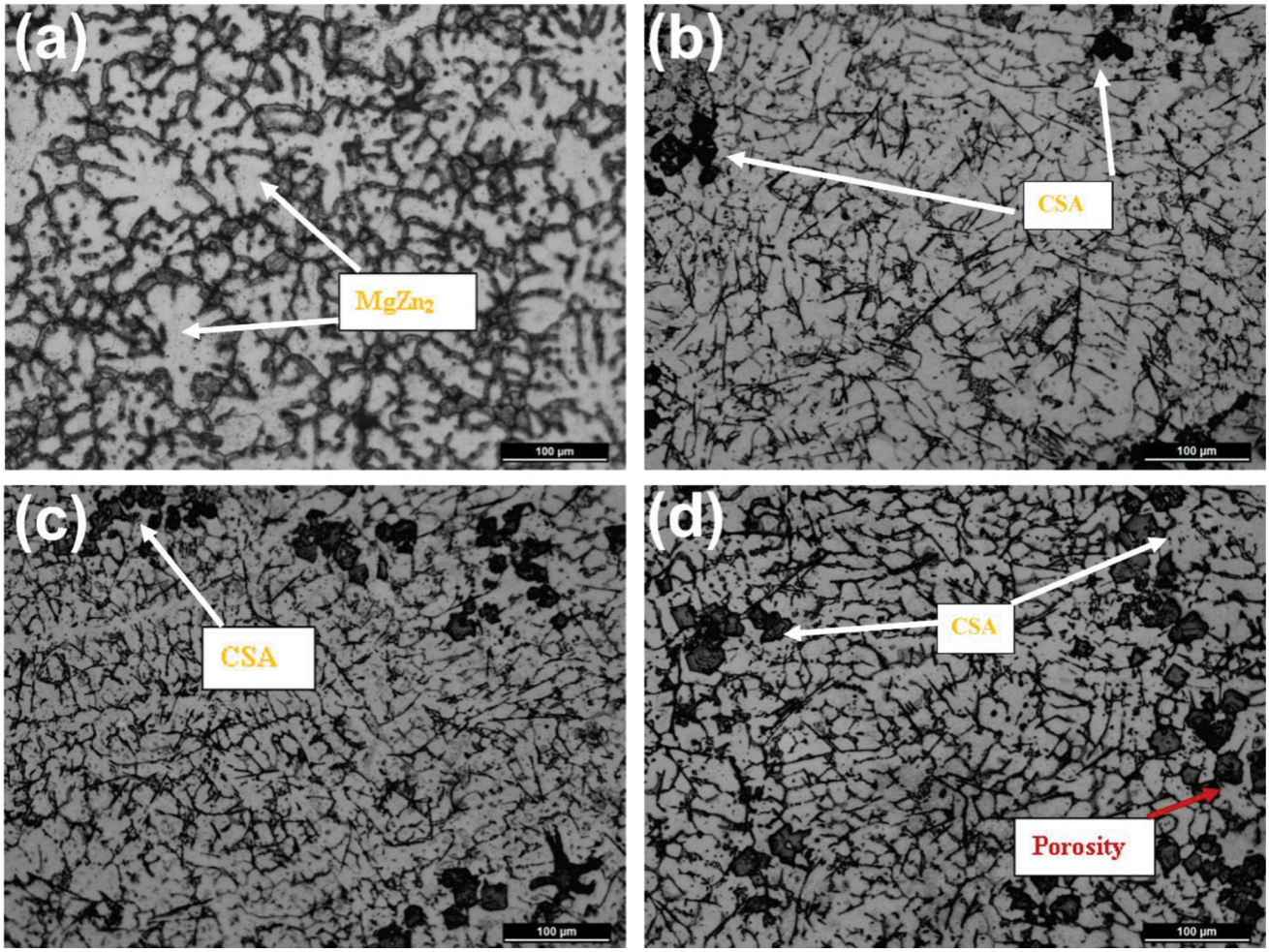

Fig. 3 Optical metallographic images of (a) AA7075, (b-d) composite specimen CSA2, CSA4 and CSA6, respectively

of Al_2O_3 and CSA. EDS spot analysis confirmed the absence of Al_4C_3 phases.

The nominal composition of the AA7075 matches the elemental analysis of the dendritic zone. Furthermore, the elemental mappings of the AA7075/Al_2O_3/CSA hybrid composites are shown in Fig. 6(a), (b), (c), (d), (e), (f), and (g), demonstrating the homogeneous dispersion of the reinforcing and alloying elements.

Figure 7 depicts the XRD patterns of both the monolithic alloy and the AA7075/Al_2O_3/CSA hybrid composite. $MgZn_2$, Al_2CuMg, and a slight fraction of Al_8Fe_2Si intermetallic phases are confirmed by XRD studies in the cast materials. During the casting of AA7075, $MgZn_2$, and Al_2CuMg intermetallic phases form naturally. For Al 7075 alloy, the Al_8Fe_2Si intermetallic phase is considered an inclusion, and precipitation of this phase in the base alloy has previously been reported (Ref 35). The existence of substantial amounts of SiO_2 and Al_2O_3 in the XRD profile is also evident in the occurrence of CSA and Al_2O_3 in the developed composite. There are no traces of secondary elements forming, indicating that the composites were successfully cast. It can only be achieved by carefully controlling the casting process parameters of reaction duration, reaction temperature, and melt stirring time.

3.2 Density and Porosity

The theoretical density was measured by the ROM, and the actual density was calculated by the Archimedes principle. The difference between theoretical density and actual density gives the porosity of the hybrid composites. The well-known densities of the AA7075 matrix, Al_2O_3, and CSA particles were 2.81, 3.97, and 1.65 g/cm^3, respectively. Figure 8 depicts the change in density with the weight percentage of reinforcements. The density of hybrid composites depends on the fractional arrangement of the number of atoms per unit volume. Moreover, the density-determining function is also how the atoms are arranged in the lattice (Ref 36). It is observed from the reading that the porosity level is between 2 and 4% for all hybrid composites. This is confirmation of the exposition of a lesser amount of porosity in the hybrid composites.

3.3 Tensile Response

When compared to the alloy, the UTS of the sample (CSA4) improved by 57.54%, but it was quite low for the composite (CSA6). The UTS improved from composite (CSA2) to composite (CSA6) before dropping to composite (CSA6). The summary of base alloy and hybrid composite of tensile test specimens is tabulated in Table 1. In composite (CSA2), the percentage elongation increases by 21.91%. The strength of the developed composite outperformed that of the AA7075 matrix

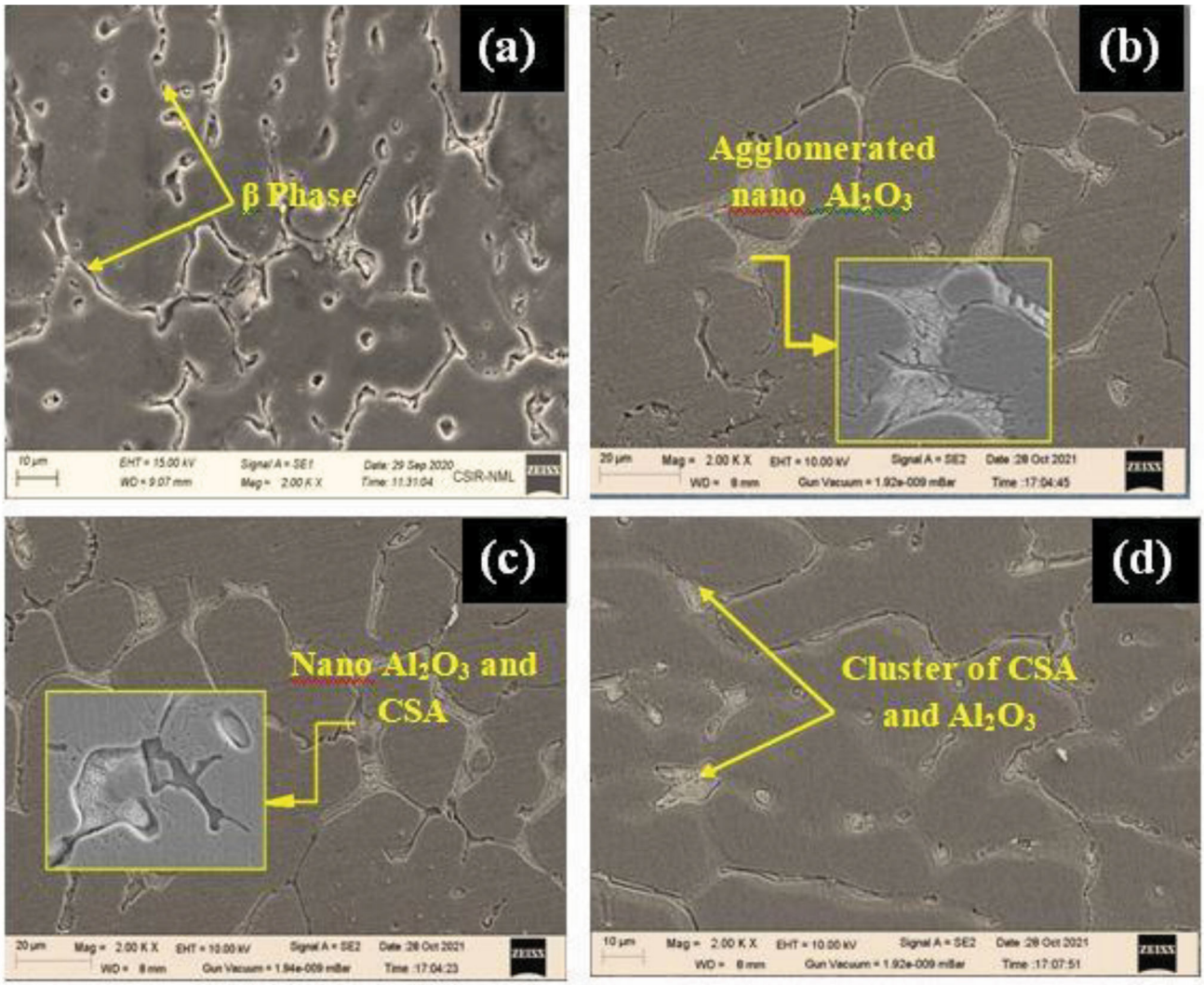

Fig. 4 SEM images of (a) AA7075, (b-d) hybrid composite specimen

due to the increased number of reinforcements. The engineering stress and strain behaviors of as-cast hybrid composites are shown in Fig. 9(a). The variation of UTS, E, and percentage elongation with a weight percentage of reinforcements is shown in Fig. 9(b). The formability, however, was hampered. Particulate agglomerations were detected in the sample (CSA6). This might explain why the tensile strength of that composite has decreased.

The elastic modulus (E) describes how stiff a material is inside the elastic limit, and the sample (CSA6) is stiffer inside the elastic region. And, because UTS indicates how much force a material can withstand before forming a neck, the composite specimen (CSA4) is the most load-bearing of the entire composite (Ref 37). The percentage elongation represents the ductility of a material; the hybrid composite (CSA2) is more ductile.

The elongations were seen to be reduced with a high content of reinforced particulate, reflecting that the ductility of hybrid composites is decreased. The homogeneously distributed reinforced particulates offer the resistance toward dislocation movement consequently the tensile strength of the hybrid composites was improved as reported by Orowan strengthening criteria (Ref 38). The higher grain fineness results in the additional ductility of the composite material. Due to the larger disarray of the lattice, grain refinement was used to resist dislocation movement, resulting in higher yield strength of the material (Ref 39). The higher the restriction, the more particles that can be present, and the particle size can be lowered to the nanoscale, as in this study. The UTS of the hybrid composite (CSA6) is improved up to 57.5% as compared to base AA7075. Kumar et al. reported similar results when combining CSA and ZrO_2 reinforcement particles to produce a hybrid composite by stir casting (Ref 40).

Figure 10 shows the fracture morphology of base alloys and hybrid composites at various $Al2O_3$ concentrations along with CSA particle concentrations. Numerous voids are equally dispersed across the fracture surface of the aluminum alloy AA7075, as shown in Fig. 10(a). The presence of deep voids suggests the fracture is ductile. The association of many voids inside the fracture surface specimens is reduced, as shown in Fig. 10(b), (c), and (d). In comparison with an unreinforced alloy, the voids are smaller. The grain refinement caused by the Al_2O_3 and CSA particles can be attributed to the smaller voids. The tensile fracture is caused by the crack initiation starting from voids and its consequent propagation, as indicated by the fracture morphology. As the crack propagates, it limits the

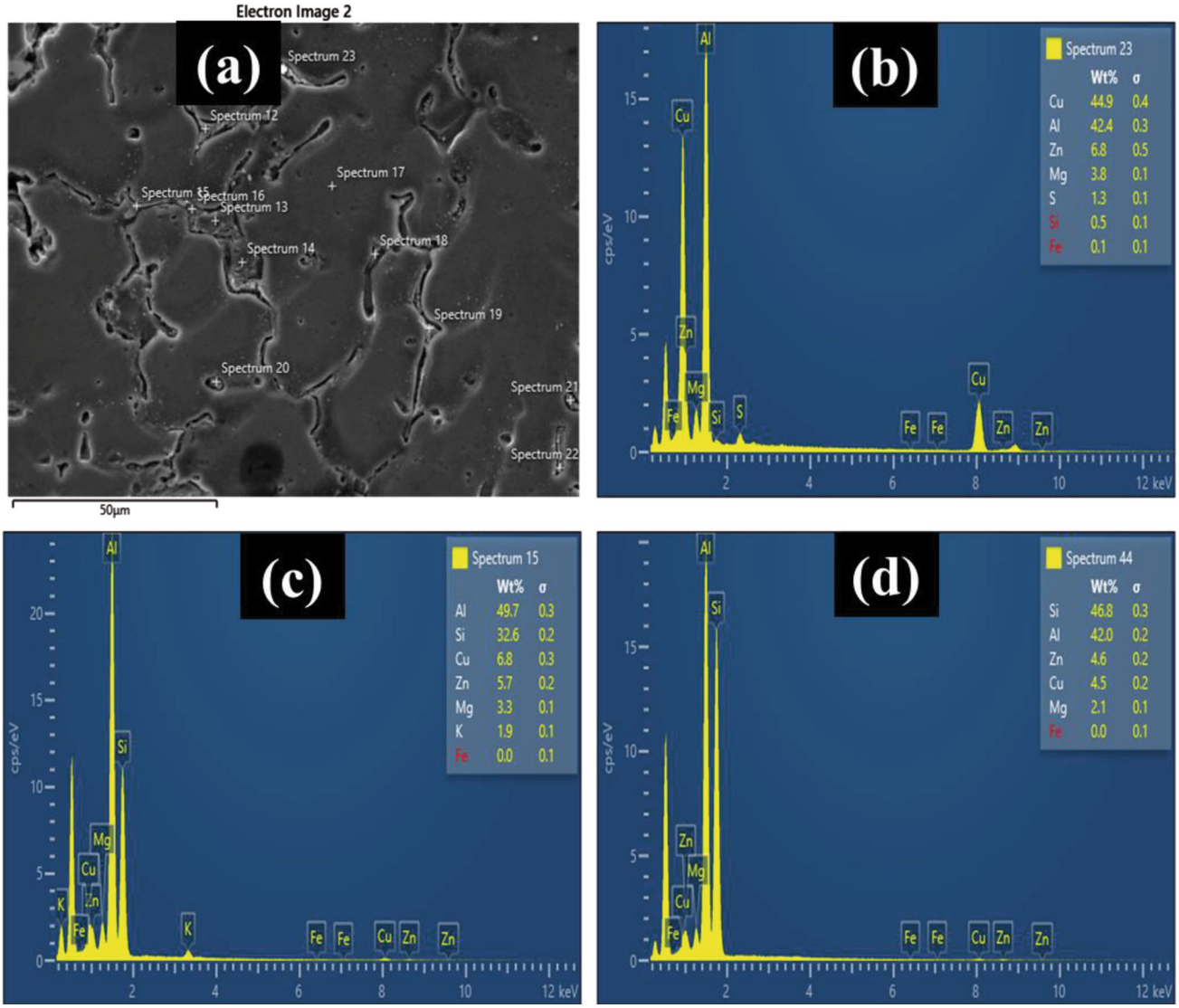

Fig. 5 (a-d) EDS analysis of AA7075/Al_2O_3/CSA hybrid composite

reinforcement by preventing the grain boundary from precipitating. The cleavage facets are formed as a result of the tensile force, which contributes to the specimens' failure (Ref 40-42). The presence of ductile shear bands on the fracture surface indicates that the composite retains ductility to a certain extent. On the fracture surface, a considerable number of fragmented CSA particles can also be seen, indicating excellent interfacial bonding.

3.4 Damping Behaviors

The damping capacity of the AA7075 was found to be 0.00539 at 1 Hz, indicating low damping. It was also seen that, as the frequency increased, the damping capability increased. Figure 11 depicts the fluctuation of damping capability with frequency for various weight percentages of reinforced particles. It can be seen from the graph that the damping capacity improves as the weight percentage of reinforcement increases. For every hybrid composite, a rising trend in damping capacity has been seen with rising frequency. Also, the damping capacity of the CSA2 sample shows similar tendencies to that of the base alloy, but with no substantial increase in damping capability. According to the literature, the damping capability of composites is higher than that of single-reinforced composites. A comparison of the damping capabilities of rice husk ash-reinforced Al composites (Ref 43) and hybrid composites was done to explain this trend. For each investigation of a different combination of reinforcement, hybrid composites have a higher damping capacity. A comparison of the damping capability of SiC reinforced aluminum composites (Ref 30) and AA7075/Al_2O_3/CSA hybrid composites was also done.

The ratio of the loss modulus to the storage modulus is called damping capacity. This relationship indicates that an increase in the value of the loss modulus or a reduction in the storage modulus will enhance the damping capacity. CSA addition reduces storage modulus, as shown in Fig. 11(b), especially for composites containing 4 and 6 weight percent of CSA. With increasing temperature, the storage modulus decreases as the bond strength decreases. The loss modulus increases with temperature as well as with Al_2O_3 and CSA additions. The temperature dependency of the elastic modulus explains the primary drop in storage modulus. The lower the

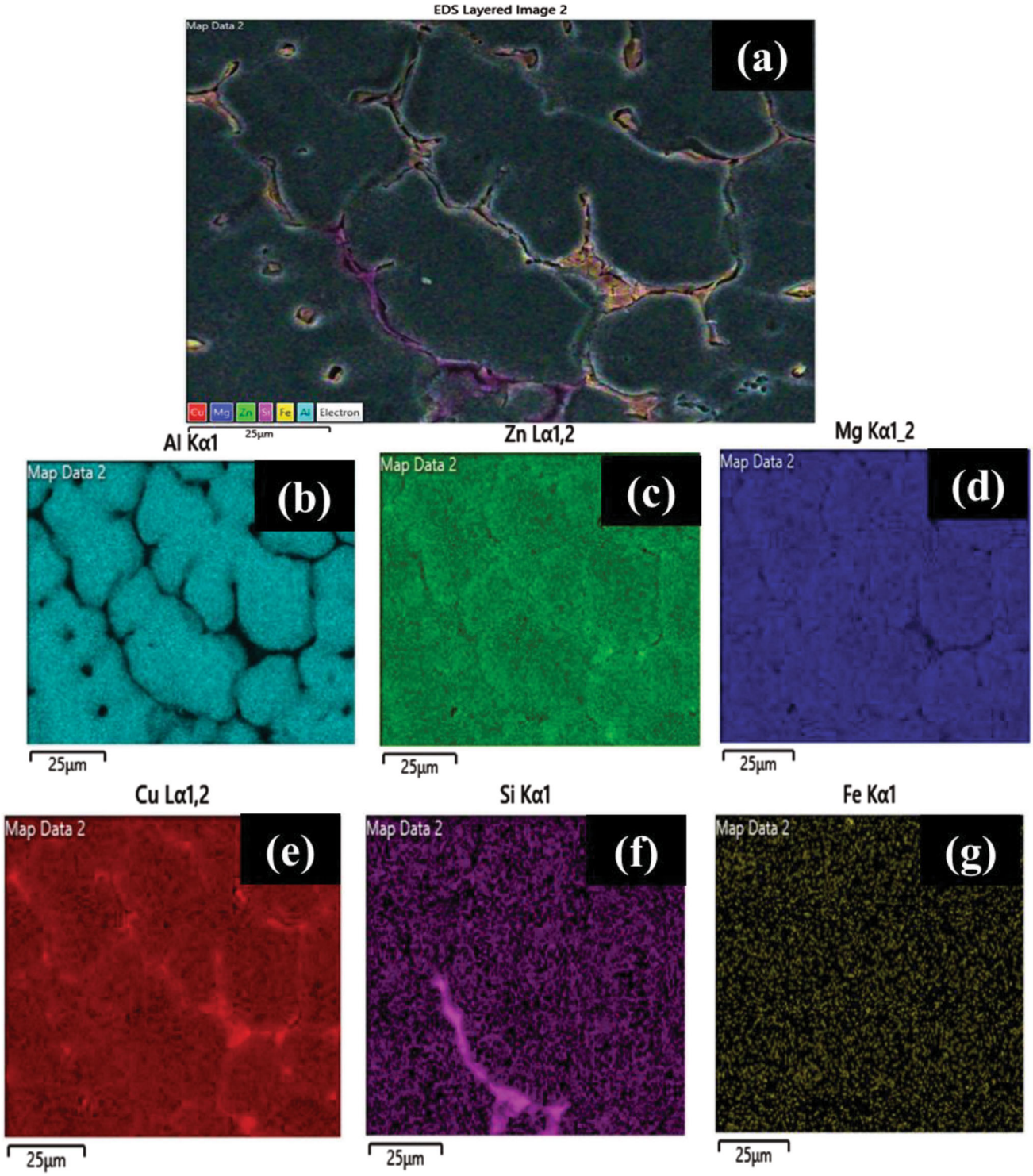

Fig. 6 (a-g) Elemental mapping of AA7075/Al_2O_3/CSA hybrid composite

frequency, the greater the reduction in storage modulus with temperature, as well as the transfer to elevated temperatures of the inflexion and confined utmost as frequency rises, indicating an Arrhenius-type relaxation rate behavior and indicating that the mechanical relaxation time decreases as temperature rises. At higher temperatures, the excitation frequency has a greater impact on the storage and loss moduli (Ref 44). Since the reinforcements are stiffer than the AA356 matrix and may promote precipitation hardening, the aluminum matrix composite is stiffer than the AA356 matrix. When compared to most of the materials investigated, the AMC's quick fall in storage modulus begins at a higher temperature, making it one of the most stable. Moreover, the precipitates and reinforcements pin the grain boundaries, and the normal relaxation peak in the matrix due to grain boundary segregation is censored in the AMC (Ref 45). Although adding 0.5 weight percent CNTs to AZ91D reduces its damping capacity at room temperature, adding 2 weight percent CNTs improves its performance.

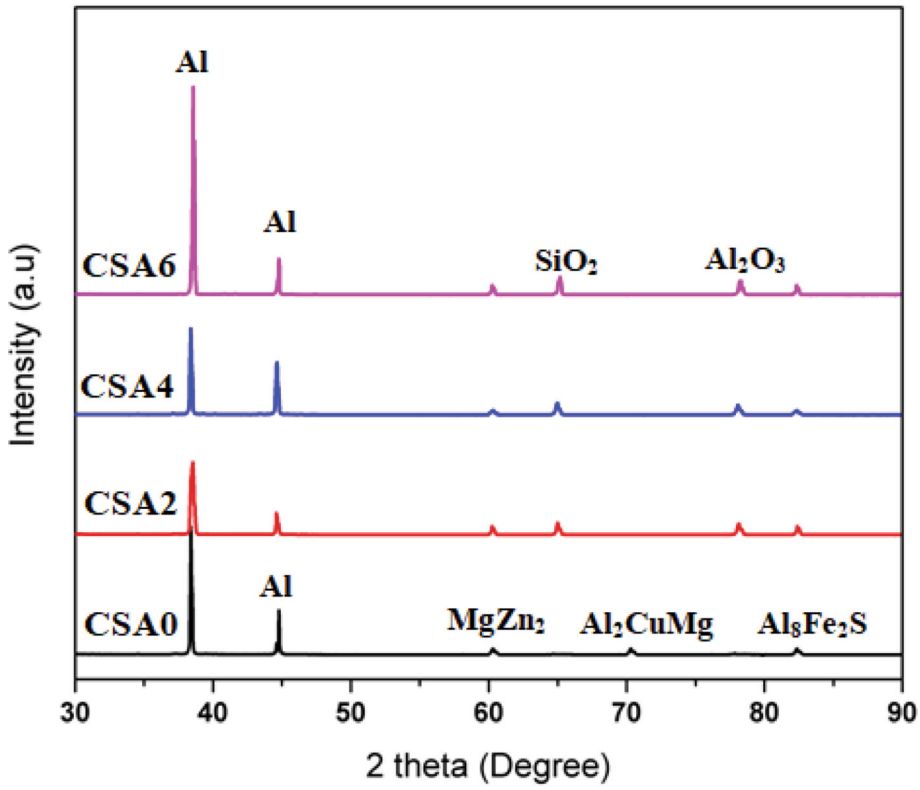

Fig. 7 XRD analysis of AA7075/Al_2O_3/CSA hybrid composite

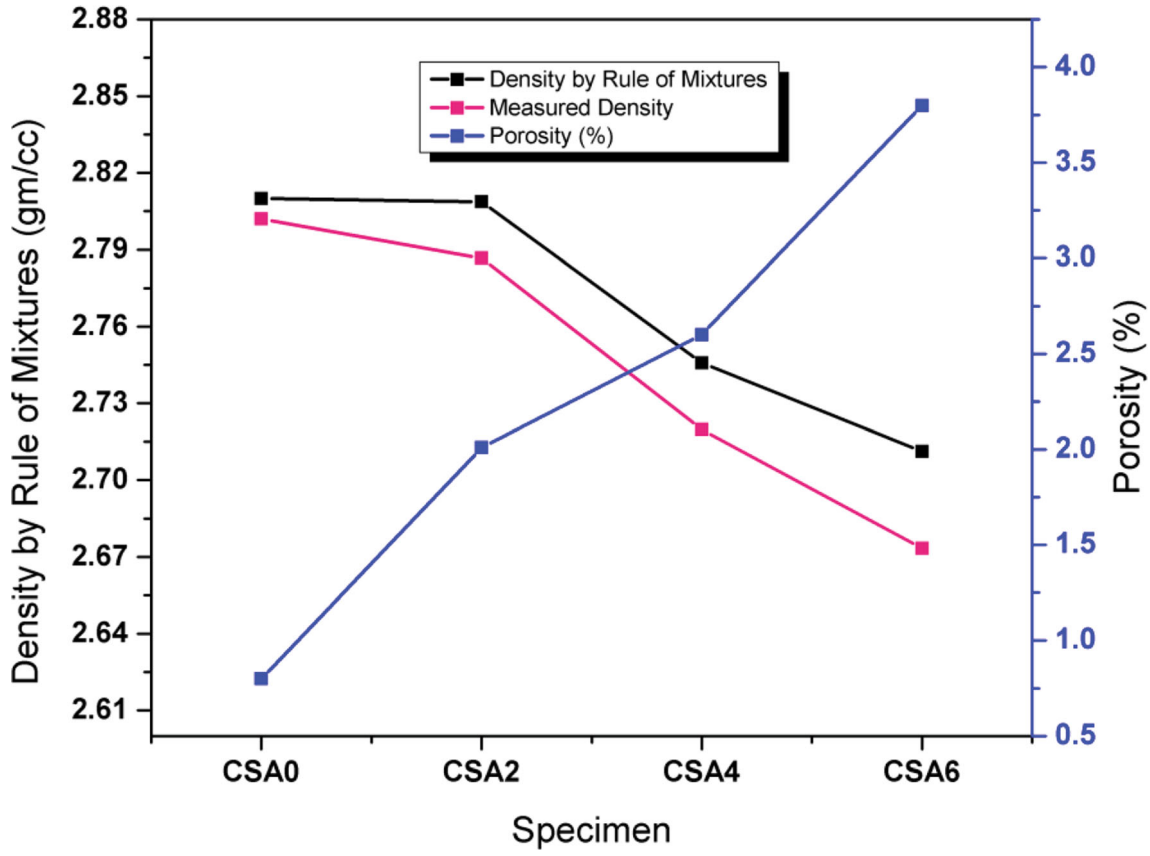

Fig. 8 Density variation of all specimens

Table 1 Summary of tensile response of base alloy and hybrid composite

Specimen	Elastic modulus, *E*, GPa	Ultimate tensile strength, UTS, MPa	Elongation, %
CSA0	56.42 ± 0.50	203 ± 6	21.67 ± 0.25
CSA2	67.06 ± 0.47	251 ± 8	26.42 ± 0.22
CSA4	75.85 ± 0.53	403 ± 9	30.31 ± 0.28
CSA6	72.31 ± 0.49	348 ± 5	23.21 ± 0.23

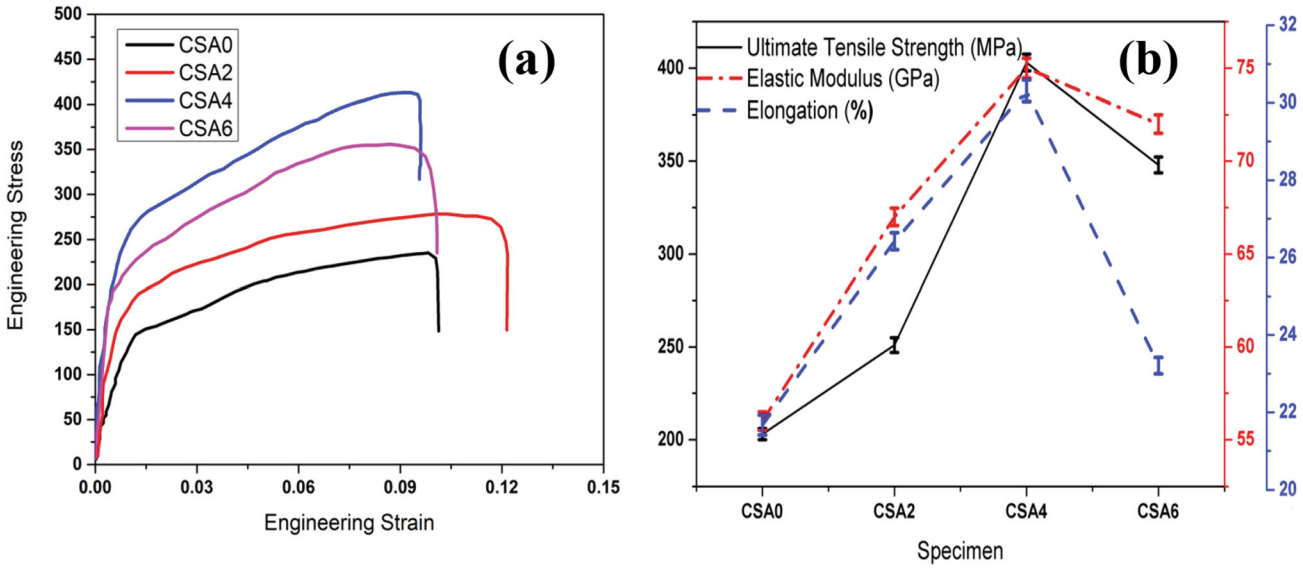

Fig. 9 (a) Engineering stress strain behaviors, (b) Variation of ultimate tensile strength, elastic modulus, percentage elongation of hybrid composites

Furthermore, regardless of the amount of CNT added, the high-temperature damping capacity improves when compared with the base aluminum alloy (Ref 46). Based on these results, it is possible to conclude that the addition of Al_2O_3 and CSA reduces the storage modulus while increasing the loss modulus. The combined action leads to damping enhancement.

3.5 Dislocation Density and Coefficient of Thermal Expansion

The strengthening of metal matrix composites has been explained by a variety of mechanisms and theories. Though the strength of a composite is not determined by a single mechanism, but by a combination of mechanisms. The strengthening mechanism in this study is mostly due to an improved dislocation density caused by a temperature difference between the reinforcement and matrix. MMCs are characterized by a huge difference in the CTE of the reinforcement and the matrix ($CTE_{AA7075} = 23.6 \times 10^{-6}$/°C, $CTE_{alumina} = 10.3 \times 10^{-6}$/°C and $CTE_{CSA} = 0.12.8 \times 10^{-6}$/°C). Thermal stresses are generated within the matrix as a result of even minor temperature changes. These stresses may be reduced in part by dislocation generation near the interfaces due to work hardening that causes dislocations to occur during the cooling of a composite, which are immobilized at the particle–matrix interface and have a high hardness that diminishes as distance from the interface increases. As a result, the generated dislocation density may be relatively significant at the interface.

The thermal expansion coefficient of composites is well known to be dependent on a number of material parameters, including composition, reinforced particulate volume fraction and distribution, matrix microstructure, in addition to residual stresses caused by CTE mismatch, volume fraction, interface strength, and porosity (Ref 47). Due to these parameters, the CTE of hybrid composites is difficult to estimate. Nevertheless, there are some analytical methods for predicting the CTE of hybrid composites, including simple mixture rules and thermo-elastic energy principles, for example the Turner and Kerner models (Ref 48).

According to the foregoing calculations, as the proportion of reinforced particles raises, the dislocation density increases from 14.2×10^{11} to 25.7×10^{11} m^3/Kg. The dislocation densities for the developed composites were computed using Burgers vector assumption of 0.32 nm for aluminum. Figure 12(a) and (b) depicts the variation of thermal expansion coefficient of each sample with a varying weight percentage of Al_2O_3 and CSA and in the ranges of temperature from 25 to 200 °C, respectively. The enhancement in CSA particle content along with an equal proportion of alumina tends to decrease the CTE of a developed composite.

The hybrid composites have a lower CTE value as compared to base AA7075. Al_2O_3 and CSA are ceramic materials with low values of CTE. When these reinforcements are incorporated into the base alloy matrix, it is expected that the values of CTE in hybrid composites will decrease. Aluminum alloys' high CTE value causes dimensional instability as temperature rises. This makes it unsuitable for end applications like

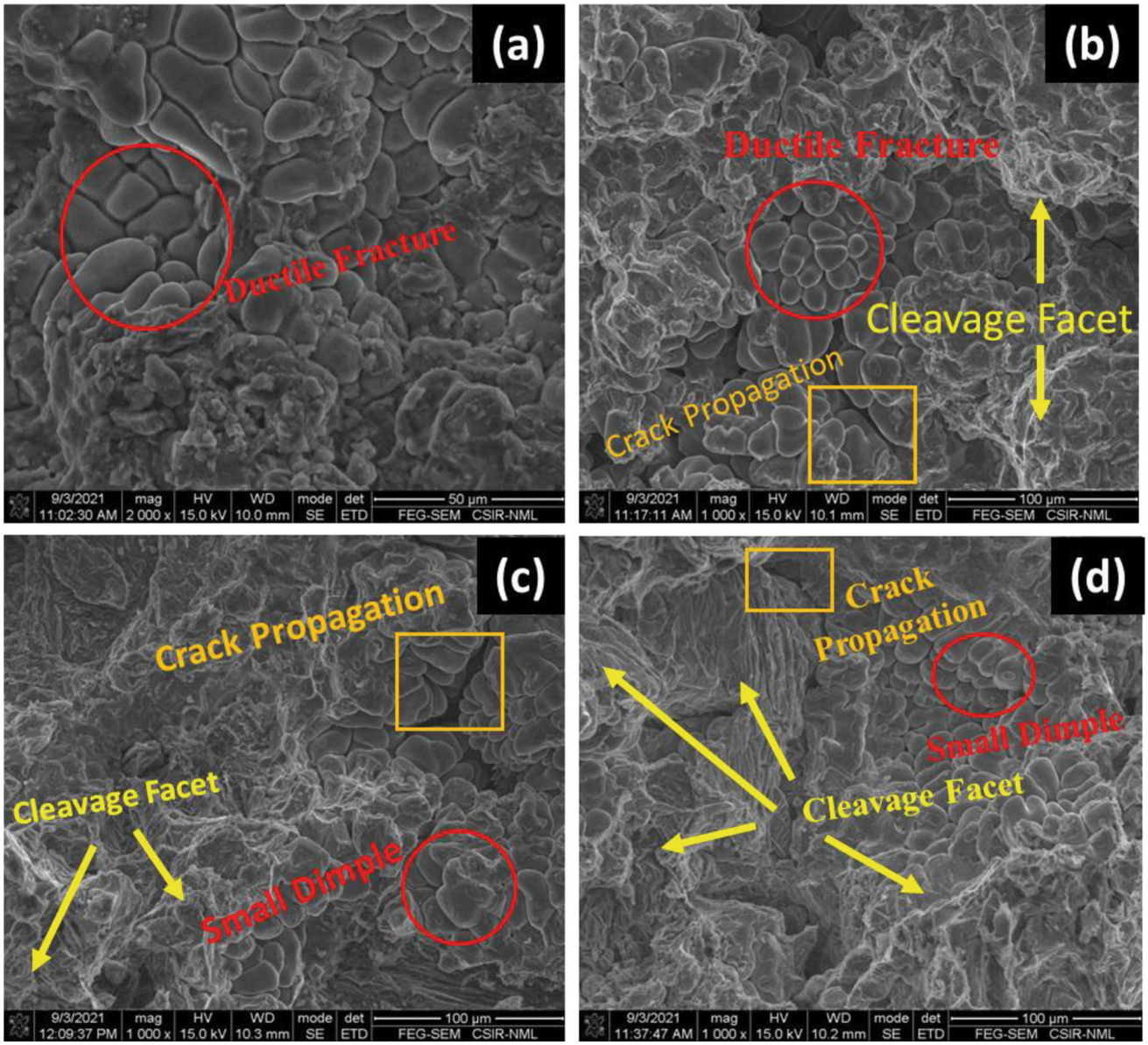

Fig. 10 Fracture morphology of AA7075/Al_2O_3/CSA hybrid composite: (a) CSA0 sample, (b) CSA2 sample, (c) CSA4 sample, and (d) CSA6 sample

electrical and electronic packaging. However, by combining reinforcements with AA7075, one can customize the CTE to meet the needs of various industry applications. Ten readings were undertaken for each sample. The result shows the efficacy of hybrid composites is higher and more dimensionally stable than base alloys in relation to changes in temperature (Ref 49). The coefficient of thermal expansion of hybrid composites is influenced by the particle size, the thermal expansion mismatch between matrix and reinforcement, and interfacial reactions.

3.6 Corrosion Behavior (Polarization Curves of Potentiodynamic Analysis)

Figure 13(a) shows the Tafels plots of the polarization curve for AA7075 monolithic alloy and hybrid composites. To investigate the corrosion dynamic layer on the projected surface, the specimens are immersed in a 3.5% sodium solution. With the inclusion of alumina and CSA particles, the potential became further negative, along with the current density dropping, as seen in Fig. 13(a). As a result, it was demonstrated that adding alumina and CSA particles to the AA7075 matrix increased corrosion resistance. The corrosion behavior was investigated by Kenneth and Olubambi (Ref 20) for an Al-Mg-Si matrix composite and it was found that rate of corrosion decreases with addition of rice husk ash and alumina in a 3.5% NaCl solution. The corrosion characteristics of the composites allegedly declined as the weight percentage of rice husk ash increased, owing to rice husk ash's lower density (0.3 g/cm^3). The potentiodynamic polarization curve depicts a decrease in current with an increase in potential in the negative direction. Loto and Babalola (Ref 50) reported similar results and well established with the explanation of reporting the corrosion behavior of Al1070 silicon carbide matrix composites.

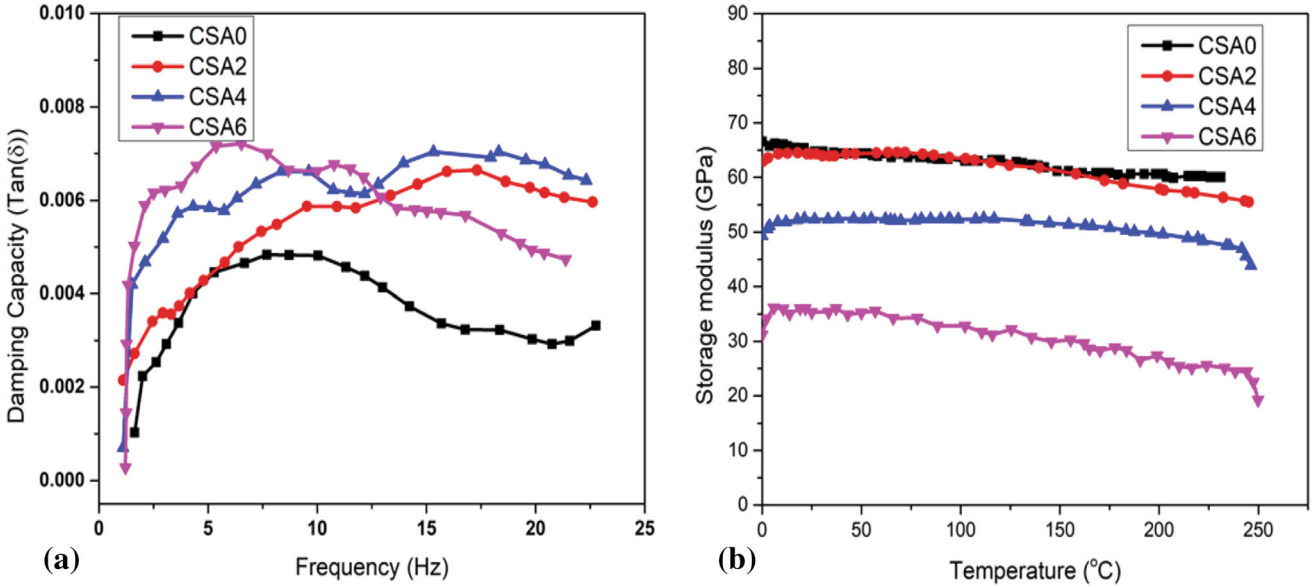

Fig. 11 (a) Variation of damping capacity with frequency at room temperature and (b) variation of storage modulus with temperature of each sample

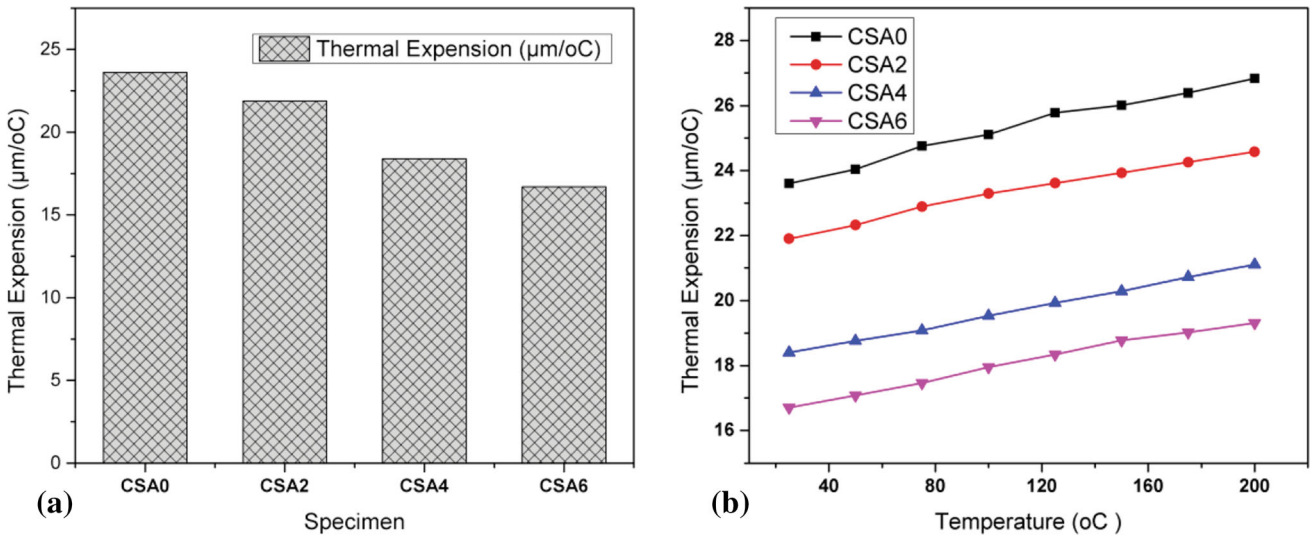

Fig. 12 (a) Variation of thermal Expansion coefficient of each sample at room temperature, (b) Thermal Expansion coefficient of each sample with varying temperature

The current density of corrosion dropped from 1.54 to 1.51 mA/cm^2 when Tafel polarization curves were plotted, confirming that adding 4 wt.% CSA along with 0.5 wt.% Al_2O_3 to AA7075 hybrid composite improves its corrosion resistance rate. There is a slight decrease in corrosion resistance for 6 wt.% CSA composites, which is seen in Fig. 13(a).

As shown in Fig. 13(b), inferior corrosion rates are related to the phase of intermetallic and the amorphous nature of reinforced composites. All cast samples have a semi-circular capacitive arc, as seen in Nyquist plots; however, there are variances in the diameter of the semi-circular arc between base alloys and hybrid composites with various and the same exposure times, respectively. The diameter of the semi-circular arc is known to reflect the corrosion resistance of the composites, with a bigger diameter suggesting stronger corrosion resistance, as reported by I. Oztürk et al. (Ref 51). The reinforced composite degradation rate reduces as the amount of CSA in the composite increases. Y. Ma et al. investigated whether the corrosion of the test alloys deteriorated first and then improved to some degree when the exposure period in the sodium chloride solution was increased. The production of $Al(OH)_3/Al_2O_3$ and corrosive layers on the specimen surfaces may be ascribed to the oxide layer lying on the specimen surfaces, the deterioration of the oxide layer for the duration of exposure in the sodium chloride solution, and the formation of Al $(OH)_3/Al_2O_3$ and corrosive layers (Ref 52). The rate of corrosion resistance of AA7075 alloy was considerably boosted by the accumulation of various weight percent (2, 4, and 6) of CSA along with 0.5 wt.% of Al_2O_3 particles, as shown by Tafels plots. The corrosion rates of the as-cast specimens after 30 days of immersion in the 3.5 weight percentage sodium chloride solution are shown in Fig. 13(c). Samuel et al. studied

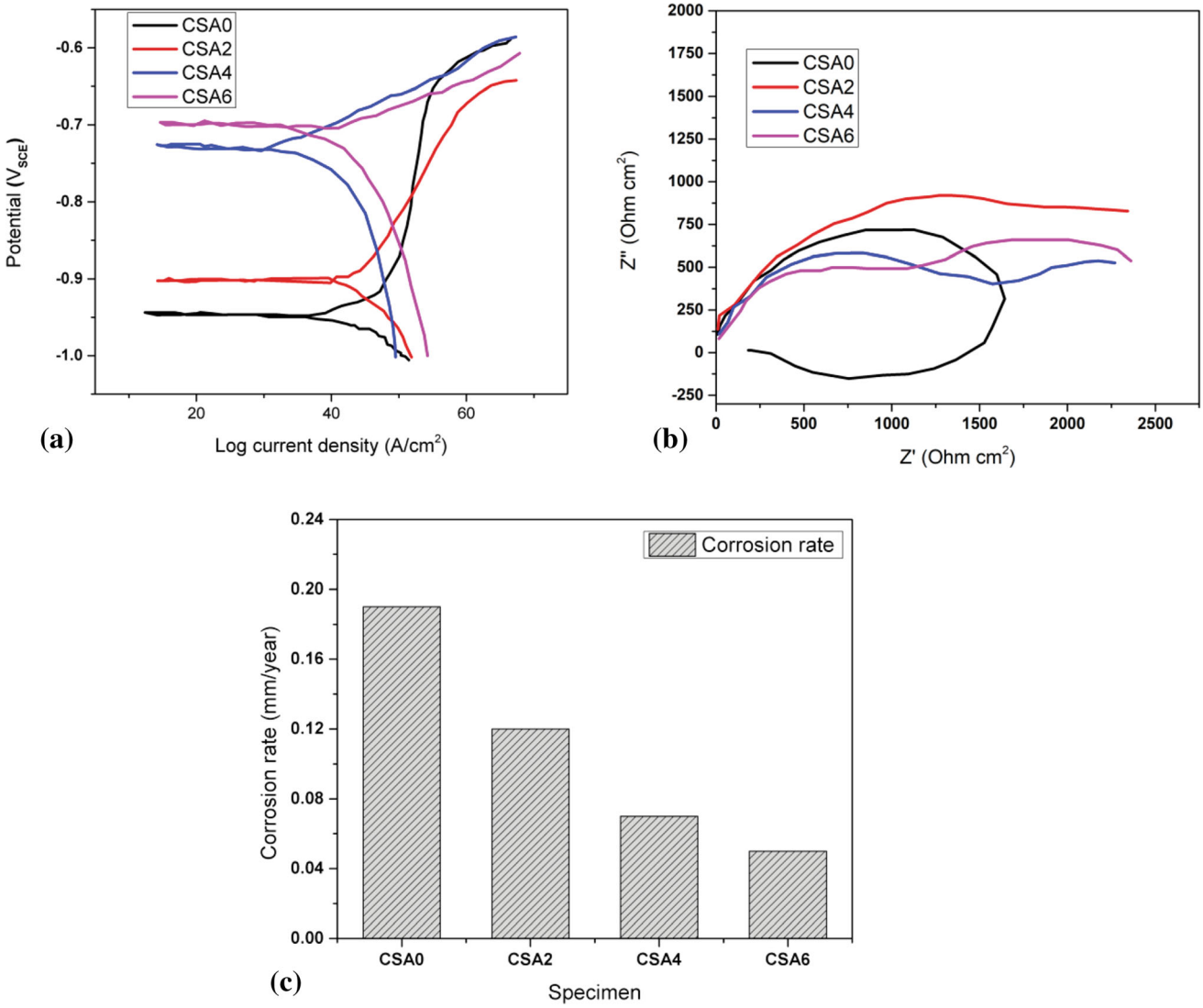

Fig. 13 (a) Potentiodynamic polarization curve, (b) Nyquist (Z′ vs. Z″) of electrochemical spectrographs and (c) Comparison of corrosion rate of as-cast specimens

corrosion behaviors of Al based composite and reported similar findings, recommending that corrosion studies of aluminum matrix composites in warm and cold conditions (except ambient temperature) be studied. This will expand their use as ship hauls, heat exchangers, and sacrificial anodes for underground pipeline protection in settings with varying ion concentrations (Ref 53). SEM and EDS analysis were used to analyze the surface morphology of AA7075 Al_2O_3/CSA hybrid composite MMC after corrosion studies. SEM micrographs and EDS analyses of corroded samples are shown in Fig. 14(a), (b), (c), and (d). The deterioration of aluminum alloys with (Al_2O_3 + CSA) is clearly caused by a regular attack in a 3.5 weight percentage of sodium chloride solution. After corrosion testing, the AA7075 sample shows pits, minor cracks, and deep precipitates, all of which indicate simultaneous metal loss on the sample surface. Because the AA7075 contains no reinforcing particles, the aluminum monolithic alloy becomes weaker, making it more susceptible to crack and pit formation. The particles of Al_2O_3 and CSA in MMCs stopped a 3.5% NaCl solution from attacking them. As shown in Fig. 14(b), (c), and (d), reinforcement in the presence of particulates improves corrosion resistance in composite specimens. The protective layer of corrosion is created on the AA7075/Al_2O_3/CSA hybrid composite surface, according to the SEM pictures.

4. Conclusions

The current study proposes the development of a hybrid MMC with nano-sized Al_2O_3 and micro-sized CSA as reinforcing particles. The ultrasonic assisted stir-casting process was used to fabricate the aforementioned composite. Based on the analysis of mechanical and thermal properties and the microstructural characterization of the cast hybrid MMC samples, the following conclusions have been made:

- Ultrasonic assisted casting played a key role in the uniform distribution of the nano-Al_2O_3, and the sample CSA4 had the maximum tensile strength, with a 59.5% as compared to AA7075 due to lesser amount of porosity. Whereas, the maximum porosity of around 3.8% was

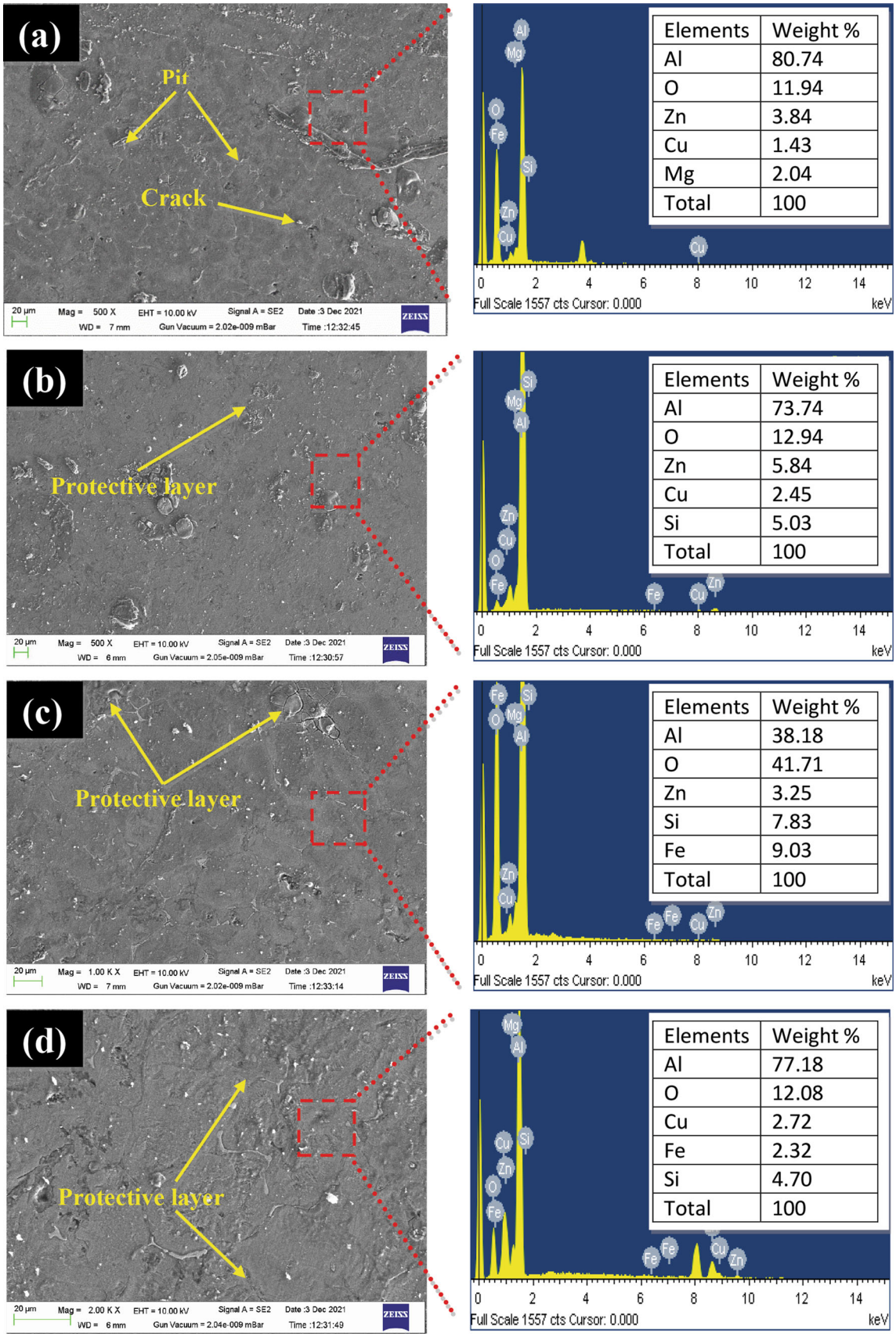

Fig. 14 SEM and corresponding EDS analysis of (a) AA7075, (b-d) hybrid composite specimen

found for the composite sample CSA6, which contained 6% by weight of CSA particles.

- The frequency-dependent damping capacity of stir-cast composites significantly increased with the variation of weight percentage of CSA. Sample CSA6 exhibited about 2 times better damping at 5 Hz, as compared to the base alloy. The significant improvement in damping behaviors is because of grain refinement along with homogenous dispersion of Al_2O_3 and CSA.
- The dislocation density increases as the reinforcing content increases, and it has an inverse relationship with CTE values.
- The inclusion of Al_2O_3 and CSA particles in AA7075 reduced the corrosion rate when exposed to potentiodynamic polarization. Hybrid composite CSA6 possesses better corrosion resistance. From Nyquist plot, it was also confirmed that the addition of Al_2O_3 and CSA particles increased the corrosion resistance of the hybrid composite.

Acknowledgments

The authors would like to appreciate the CSIR-National Metallurgical Laboratory, Jamshedpur, India for providing the facilities for material characterizations. The authors would also like to thank Delhi Technological University (DTU), Delhi, India for providing the testing facilities.

Conflict of interest

The authors declare that they have no conflict of interest.

Ethics Approval and Consent to Participate

Not applicable.

References

1. P. Samal, P.R. Vundavilli, A. Meher and M.M. Mahapatra, Recent Progress in Aluminum Metal Matrix Composites: A Review on Processing, Mechanical and Wear Properties, *J. Manuf. Process.*, 2020, **59**, p 131–152.
2. A.K. Singh, S. Soni and R.S. Rana, A Critical Review on Synthesis of Aluminum Metallic Composites through Stir Casting: Challenges and Opportunities, *Adv. Eng. Mater.*, 2020, **22**(10), p 2000322.
3. P.L. Kumar, A. Lombardi, G. Byczynski, S.V.S. NarayanaMurty, B.S. Murty and L. Bichler, Recent Advances in Aluminium Matrix Composites Reinforced with Graphene-Based Nanomaterial: A Critical Review, *Prog. Mater. Sci.*, 2022, **128**, p 100948.
4. S. Suresh, G. HarinathGowd and M.L.S. Kumar, Mechanical and Wear Behavior of Al 7075/Al_2O_3/SiC/mg Metal Matrix Nanocomposite by Liquid State Process, *Adv. Compos. Hybrid Mater.*, 2019, **2**(3), p 530–539.
5. X. Yu, H. Bakhtiari, J. Zhou, M.O. Bidgoli and K. Asemi, Investigating the Effect of Reinforcing Particles Size and Content on Tensile and Fatigue Properties of Heat-Treated Al7075-SiC Composites Fabricated by the Stir Casting Method, *JOM*, 2022, **74**(5), p 1859–1869.
6. T.P. Reddy, S. Jaya Kishore, P. CharanTheja and P. Punna Rao, Development and Wear Behavior Investigation on Aluminum-7075/B4C/Fly Ash Metal Matrix Composites, *Adv. Compos. Hybrid Mater.*, 2020, **3**(2), p 255–265.
7. A. Baradeswaran and A. ElayaPerumal, Study on Mechanical and Wear Properties of Al 7075/Al_2O_3/Graphite Hybrid Composites, *Compos. Part B Eng.*, 2014, **56**, p 464–471.
8. S.V. Prasad and R. Asthana, Aluminum Metal-Matrix Composites for Automotive Applications: Tribological Considerations, *Tribol. Lett.*, 2004, **17**(3), p 445–453.
9. R. Manikandan and T.V. Arjunan, Studies on Micro Structural Characteristics, Mechanical and Tribological Behaviours of Boron Carbide and Cow Dung Ash Reinforced Aluminium (Al 7075) Hybrid Metal Matrix Composite, *Compos. B Eng.*, 2020, **183**, p 107668.
10. P. Saini and P.K. Singh, Physical, Morphological, and Mechanical Characterization of Al-4032/GMP Composite Fabricated through Stir Casting, *JOM*, 2022, **74**(4), p 1340–1349.
11. C. Kannan and R. Ramanujam, Comparative Study on the Mechanical and Microstructural Characterisation of AA 7075 Nano and Hybrid Nanocomposites Produced by Stir and Squeeze Casting, *J. Adv. Res.*, 2017, **8**(4), p 309–319.
12. S. Liu, Y. Wang, T. Muthuramalingam and G. Anbuchezhiyan, Effect of B4C and MOS_2 Reinforcement on Micro Structure and Wear Properties of Aluminum Hybrid Composite for Automotive Applications, *Compos. Part B Eng.*, 2019, **176**, p 107329.
13. A. Ramanathan, P.K. Krishnan and R. Muraliraja, A Review on the Production of Metal Matrix Composites through Stir Casting–Furnace Design, Properties, Challenges, and Research Opportunities, *J. Manuf. Process.*, 2019, **42**, p 213–245.
14. V.S. Aigbodion, S.B. Hassan, E.T. Dauda and R.A. Mohammed, The Development of Mathematical Model for the Prediction of Ageing Behaviour for Al-Cu-Mg/Bagasse Ash Particulate Composites, *J. Miner. Mater. Charact. Eng.*, 2010, **9**(10), p 907–917.
15. A. Kumar, R.C. Singh and R. Chaudhary, Investigation of Nano-Al_2O_3 and Micro-coconut Shell Ash (CSA) Reinforced AA7075 Hybrid Metal–Matrix Composite using Two-Stage Stir Casting, *Arab. J. Sci. Eng.*, 2022, **47**, p 15559–15573.
16. O.B. Fatile, J.I. Akinruli and A.A. Amori, Microstructure and Mechanical Behaviour of Stir-Cast Al-Mg-Sl Alloy Matrix Hybrid Composite Reinforced with Corn Cob Ash and Silicon Carbide, *Int. J. Eng. Technol. Innov.*, 2014, **4**(4), p 251.
17. I.M.R. Najjar, A.M. Sadoun, M.A. Elaziz, A.W. Abdallah, A. Fathy and A.H. Elsheikh, Predicting Kerf Quality Characteristics in Laser Cutting of Basalt Fibers Reinforced Polymer Composites using Neural Network and Chimp Optimization, *Alex. Eng. J.*, 2022, **61**(12), p 11005–11018.
18. R.S.S. Raju, M.K. Panigrahi, R.I. Ganguly and G. Srinivasa Rao, Tribological Behaviour of Al-1100-Coconut Shell Ash (CSA) Composite at Elevated Temperature, *Tribol. Int.*, 2019, **129**, p 55–66.
19. J.E. Oghenevweta, V.S. Aigbodion, G.B. Nyior and F. Asuke, Mechanical Properties and Microstructural Analysis of Al-Si-Mg/Carbonized Maize Stalk Waste Particulate Composites, *J. King Saud Univ. Eng. Sci.*, 2016, **28**(2), p 222–229.
20. K.K. Alaneme and P.A. Olubambi, Corrosion and Wear Behaviour of Rice Husk Ash—Alumina Reinforced Al-Mg-Si Alloy Matrix Hybrid Composites, *J. Mater. Res. Technol.*, 2013, **2**(2), p 188–194.
21. R. Siva Sankara Raju, M.K. Panigrahi, R.I. Ganguly and G. Srinivasa Rao, Investigation of Tribological Behavior of a Novel Hybrid Composite Prepared with Al-Coconut Shell Ash Mixed with Graphite, *Metall. Mater. Trans. A*, 2017, **48**(8), p 3892–3903.
22. S.C. Tjong, Recent Progress in the Development and Properties of Novel Metal Matrix Nanocomposites Reinforced with Carbon Nanotubes and Graphenenanosheets, *Mater. Sci. Eng. R. Rep.*, 2013, **74**(10), p 281–350.
23. P. Madhukar, N. Selvaraj, C.S.P. Rao and G.B. Veeresh Kumar, Fabrication and Characterization Two Step Stir Casting with Ultrasonic Assisted Novel AA7150-hBN Nanocomposites, *J. Alloys Compd.*, 2020, **815**, p 152464.
24. A.M. Sadoun, I.M.R. Najjar, M.S. Abd-Elwahed and A. Meselhy, Experimental Study on Properties of Al–Al_2O_3 Nanocomposite Hybridized by Graphene Nanosheets, *J. Market. Res.*, 2020, **9**(6), p 14708–14717.
25. H. Su, W. Gao, Z. Feng and Z. Lu, Processing, Microstructure and Tensile Properties of Nano-sized Al_2O_3 Particle Reinforced Aluminum Matrix Composites, *Mater. Des. (1980–2015)*, 2012, **36**, p 590–596.
26. ThellaBabu Rao, Microstructural, Mechanical, and Wear Properties Characterization and Strengthening Mechanisms of Al7075/SiCnp Composites Processed through Ultrasonic Cavitation Assisted Stir-Casting, *Mater. Sci. Eng. A*, 2021, **805**, p 140553.
27. O.B. Bembalge and S.K. Panigrahi, Development and Strengthening Mechanisms of Bulk Ultrafine Grained AA6063/SiC Composite Sheets

with Varying Reinforcement Size Ranging from Nano to Micro Domain, *J. Alloys Compd.*, 2018, **766**, p 355–372.
28. X. Meng, D. Zhang, W. Zhang, C. Qiu and D. Chen, Achieving High Damping Capacity and Strength Simultaneously in a High-Zinc Aluminum Alloy via Melt Spinning and Hot Extrusion, *Mater. Sci. Eng. A*, 2022, **833**, p 142376.
29. S. Madeira, O. Carvalho, V.H. Carneiro, D. Soares, F.S. Silva and G. Miranda, Damping Capacity and Dynamic Modulus of Hot Pressed AlSi Composites Reinforced with Different SiC Particle Sized, *Compos. B Eng.*, 2016, **90**, p 399–405.
30. R. Bauri and M.K. Surappa, Damping Behavior of Al-Li-SiCp Composites Processed by Stir Casting Technique, *Metall. Mater. Trans. A*, 2005, **36**(3), p 667–673.
31. W.A. Uju and I.N.A. Oguocha, A Study of Thermal Expansion of Al-Mg Alloy Composites Containing Fly Ash, *Mater. Des.*, 2012, **33**, p 503–509.
32. M. Rahsepar and H. Jarahimoghadam, The Influence of Multipass Friction Stir Processing on the Corrosion Behavior and Mechanical Properties of Zircon-Reinforced Al Metal Matrix Composites, *Mater. Sci. Eng. A*, 2016, **671**, p 214–220.
33. R. Bertolini, E. Simonetto, L. Pezzato, A. Fabrizi, A. Ghiotti and S. Bruschi, Mechanical and Corrosion Resistance Properties of AA7075-T6 Sub-zero Formed Sheets, *Int. J. Adv. Manuf. Technol.*, 2021, **115**, p 1–24.
34. A. Bakkar and S. Ataya, Corrosion Behaviour of Stainless Steel Fibre-Reinforced Copper Metal Matrix Composite with Reference to Electrochemical Response of Its Constituents, *Corros. Sci.*, 2014, **85**, p 343–351.
35. S. Sardar, S.K. Karmakar and D. Das, High Stress Abrasive Wear Characteristics of Al 7075 Alloy and $7075/Al_2O_3$ Composite, *Measurement*, 2018, **127**, p 42–62.
36. K.P. Kumar, M. Gopi Krishna, J. Babu Rao and N.R.M.R. Bhargava, Fabrication and Characterization of Aluminium–High Entropy Alloy Composites, *J. Alloys Compd.*, 2015, **640**, p 421–427.
37. R. Escalera-Lozano, C.A. Gutiérrez, M.A. Pech-Canul and M.I. Pech-Canul, Degradation of Al/SiCp Composites Produced with Rice-Hull Ash and Aluminum Cans, *Waste Manag.*, 2008, **28**(2), p 389–395.
38. J. Zhu, W. Jiang, G. Li, F. Guan, Yu. Yang and Z. Fan, Microstructure and Mechanical Properties of SiCnp/Al6082 Aluminum Matrix Composites Prepared by Squeeze Casting Combined with Stir Casting, *J. Mater. Process. Technol.*, 2020, **283**, p 116699.
39. Z. Zhang and D.L. Chen, Contribution of Orowan Strengthening Effect in Particulate-Reinforced Metal Matrix Nanocomposites, *Mater. Sci. Eng., A*, 2008, **483**, p 148–152.
40. K.R. Kumar, T. Pridhar and V.S. SreeBalaji, Mechanical Properties and Characterization of zirconium oxide (ZrO_2) and Coconut Shell Ash (CSA) Reinforced Aluminium (Al 6082) Matrix Hybrid Composite, *J. Alloys Compd.*, 2018, **765**, p 171–179.
41. J.-Q. Han, J.-S. Wang, M.-S. Zhang and K.-M. Niu, Relationship Between Amounts of Low-Melting-Point Eutectics and Hot Tearing Susceptibility of Ternary Al-Cu-Mg Alloys during Solidification, *Trans. Nonferrous Met. Soc. China*, 2020, **30**(9), p 2311–2325.
42. W. Jiang, J. Zhu, G. Li, F. Guan, Yu. Yang and Z. Fan, Enhanced Mechanical Properties of 6082 Aluminum Alloy via SiC Addition Combined with Squeeze Casting, *J. Mater. Sci. Technol.*, 2021, **88**, p 119–131.
43. D.S. Prasad and A.R. Krishna, Effect of T6 Heat Treatment on Damping Characteristics of Al/RHA Composites, *Bull. Mater. Sci.*, 2012, **35**(6), p 989–995.
44. J.I. Rojas and D. Crespo, Modeling of the Effect of Temperature, Frequency, and Phase Transformations on the Viscoelastic Properties of AA 7075-T6 and AA 2024-T3 Aluminum Alloys, *Metall. and Mater. Trans. A.*, 2012, **43**(12), p 4633–4646.
45. J.I. Rojas, B.V. Siva, K. Lal Sahoo and D. Crespo, Viscoelastic Behavior of a Novel Aluminum Metal Matrix Composite and Comparison with Pure Aluminum, Aluminum Alloys, and a Composite made of Al-Mg-Si Alloy Reinforced with SiC Particles, *J. Alloys Compd.*, 2018, **744**, p 445–452.
46. M. Ebrahimi, Li. Zhang, Q. Wang, H. Zhou and W. Li, Damping Characterization and Its Underlying Mechanisms in CNTs/AZ91D Composite Processed by Cyclic Extrusion and Compression, *Mater. Sci. Eng. A*, 2021, **821**, p 141605.
47. H. Hatta, T. Takei and M. Taya, Effects of Dispersed Microvoids on Thermal Expansion Behavior of Composite Materials, *Mater. Sci. Eng., A*, 2000, **285**(1–2), p 99–110.
48. Ke. Chu, X.-H. Wang, Y.-B. Li, D.-J. Huang, Z.-R. Geng, X.-L. Zhao, H. Liu and Hu. Zhang, Thermal Properties of Graphene/Metal Composites with Aligned Graphene, *Mater. Des.*, 2018, **140**, p 85–94.
49. T. Wang, T. Fan, D. Zhang, G. Zhang and D. Xiong, Preparation and Thermal Properties of Metal Matrix Composites with Wood-Structure, *Mater. Des.*, 2008, **29**(6), p 1275–1279.
50. R.T. Loto and P. Babalola, Corrosion polarization behavior and microstructural analysis of AA1070 aluminium silicon carbide matrix composites in acid chloride concentrations, *Cogent Eng.*, 2017, **4**(1), p 1422229.
51. İ Öztürk, G.H. Ağaoğlu, E. Erzi, D. Dispinar and G. Orhan, Effects of Strontium Addition on the Microstructure and Corrosion Behavior of A356 Aluminum Alloy, *J. Alloys Compd.*, 2018, **763**, p 384–391.
52. Y. Ma, Y. Liu and M. Wang, Microstructures and Corrosion Resistances of Hypoeutectic Al-6.5Si-0.45Mg Casting Alloy with Addition of Sc and Zr, *Mater. Chem. Phys.*, 2022, **276**, p 125321.
53. S.O. Akinwamide, B.T. Abe, O.J. Akinribide, B.A. Obadele and P.A. Olubambi, Characterization of Microstructure, Mechanical Properties and Corrosion Response of Aluminium-Based Composites Fabricated via Casting—A Review, *Int. J. Adv. Manuf. Technol.*, 2020, **109**(3), p 975–991.